Research Square

Preprints are preliminary reports that have not undergone peer review.
They should not be considered conclusive, used to inform clinical practice,
or referenced by the media as validated information.

Directional mesh sensitivity and neural-operator defect correction for weld pool prediction in laser manufacturing

Wenbo Zhou
Chinese Academy of Sciences
Jiatong Li
National University of Singapore
Hanwei Wang
Chinese Academy of Sciences
Lele Hu
Chinese Academy of Sciences
Xuyang Chen
chenxy.2018@tsinghua.org.cn
Chinese Academy of Sciences
Heng Jiang
Chinese Academy of Sciences

Article

Keywords:

Posted Date: November 20th, 2026

DOI: https://doi.org/10.21203/rs.3.rs-11359433/v1

License: This work is licensed under a Creative Commons Attribution 4.0 International License.
Read Full License

Additional Declarations: No competing interests reported.

Directional mesh sensitivity and neural-operator defect correction for weld pool prediction in laser manufacturing

Wenbo Zhou[1,3,4], Jiatong Li[2], Hanwei Wang[3,4], Lele Hu[3,4], Xuyang Chen[3,5*], Heng Jiang[1*]

[1]Key Laboratory of Microgravity, Institute of Mechanics, Chinese Academy of Sciences, Beijing, 100190, China.
[2]School of Computing, National University of Singapore, Singapore, 117576, Singapore.
[3]Institute of Engineering Thermophysics, Chinese Academy of Sciences, Beijing, 100190, China.
[4]University of Chinese Academy of Sciences, Beijing, 100049, China.
[5]Institute of Applied Materials, Microstructure Modelling and Simulation, Karlsruhe Institute of Technology, Karlsruhe, 76344, Germany.

*Corresponding author(s). E-mail(s): chenxy.2018@tsinghua.org.cn; hengjiang@imech.ac.cn;

Abstract

Melt-pool geometry in laser manufacturing is set by three-dimensional heat, flow and solute transport. Finite-volume simulation is the reference tool, but equal refinement in all three directions is prohibitive, and pool quantities are not equally sensitive to each direction. A directional resolution audit is therefore carried out on a finite-volume melt-pool model. The material enters through its thermophysical properties, and the numerical experiments use experimentally validated parameters. On 156 converged cases, doubling the number of J nodes reduces the melt-width error by 1.27% and the liquid-volume error by 2.39%; the same refinement of I or K yields only 0.03% and 0.16%, about a 40-fold difference. This matches the Marangoni-dominated free-surface viscous shear layer. A Fourier neural operator then supplies the coarse-to-fine correction. On 48 unseen cases on the $73 \times 8 \times 20$ mesh, the melt-width error is reduced by 53.9% and the liquid-volume error by 59.6%. Resolution should therefore follow directional

sensitivity rather than equal refinement. With the conservative solve kept on an affordable mesh and a neural operator restoring the resolution that governs pool geometry, the computational budget is reduced substantially.

Keywords: hybrid laser–MIG welding, weld-pool geometry, direction-dependent mesh refinement, Fourier neural operator, laser manufacturing

Nomenclature

Symbol	Meaning	Unit
$C, C_{\max}$	magnesium mass fraction and its liquid-region peak	–
C_p	specific heat	$\mathrm{J\,kg^{-1}\,K^{-1}}$
D	solute diffusivity in the liquid	$\mathrm{m^2\,s^{-1}}$
D_{p}	melt-pool depth (penetration)	m
f_ℓ, f_s	liquid, solid fraction	–
h	sensible enthalpy	$\mathrm{J\,kg^{-1}}$
I, J, K	mesh indices along the weld, half-width and thickness	–
k	thermal conductivity	$\mathrm{W\,m^{-1}\,K^{-1}}$
L	melt-pool length	m
Le, Pr, Re	Lewis, Prandtl and Reynolds numbers	–
m_I, m_J, m_K	retained spectral resolution in each direction	–
P, V	laser power, travel speed	W, $\mathrm{m\,s^{-1}}$
Pe_T, Pe_C	thermal, solutal Peclet numbers	–
T, T_s, T_l	temperature, solidus, liquidus	K
U	field vector (u, v, w, T, C)	–
$W, W/2$	melt-pool width, half-width	m
$\mathcal{V}_\ell$	liquid volume	$\mathrm{m^3}$
α, ν	thermal diffusivity, kinematic viscosity	$\mathrm{m^2\,s^{-1}}$
$\delta_T, \delta_\nu, \delta_C$	thermal, viscous and solutal boundary layers	m
$\ell_I, \ell_J, \ell_{\mathrm{mushy}}$	thermal-wake, recirculation-cell and mushy-front lengths	m
$\mathcal{I}, \mathcal{R}_\theta$	trilinear lifting, defect correction	–
Ω_ℓ	liquid region, $T \geq T_s$	–
$\Delta x, \Delta y, \Delta z$	near-weld median spacing	m

1 Introduction

In laser manufacturing, the melt pool delivers energy and filler metal into the workpiece. Its geometry and composition set the penetration, bead width, bead length, reinforcement and dilution, and thereby the joint properties. Hybrid laser–MIG welding combines a concentrated laser keyhole with the heat and mass sources of a filler wire in a single pool, and thereby gives metallic structures deeper penetration, higher travel speed and better gap bridging than either process alone [1, 2]. These engineering quantities are set by three-dimensional heat, flow and solute transport in the weld pool.

Melt-pool geometry arises from the coupling of Marangoni and electromagnetic forces, melting and solidification, droplet impingement and free-surface deformation, and is therefore predicted by three-dimensional thermo-fluid-solute models rather than by conduction-only analyses [3, 4]. Three-dimensional transport in keyhole and hybrid welding [5–8], heat and flow in laser spot and keyhole welding [9, 10], and aluminium melt-pool geometry and solidification [11, 12] all attribute melt width, penetration and composition to conservation of energy, momentum and mass. Models of the same family have been used for MIG welding of thin aluminium plate [13], laser welding with powder feeding [14], laser–MIG hybrid welding [15, 16] and melt-pool evolution in directed energy deposition [17, 18]. The numerical experiments use a finite-volume model that has already been validated against the measured weld cross-section and the magnesium and zinc EDS profiles [19].

The obstacle is computational cost. Equal refinement in all three directions overruns the node budget, whereas melt width and penetration are not equally sensitive to resolution in each direction. A weld pool is geometrically anisotropic: the thermal wake is stretched by convection along the travel direction, Marangoni recirculation occupies the half-width, and solidification proceeds through the thickness [6, 7, 20]. In melt-pool simulation, a finer mesh usually brings the geometry and the physical fields closer to a reference solution, but increasing the node count raises the cost rapidly, and equal refinement in all three directions is often unaffordable. A common practice is therefore to refine the near-weld region and coarsen the far field; anisotropic adaptation has also been used for welding thermo-metallurgy and for CFD [21–23]. These strategies ease the budget pressure, yet they still do not identify which direction limits melt width or penetration. Order-of-magnitude estimates alone still tend to waste part of the computational budget. This paper does not restate the general claim that the mesh should be finer or anisotropic. It provides a directional resolution audit of the engineering quantities, so that the node budget follows the directional sensitivity of melt width and penetration, the conservative solve is kept on an affordable mesh, and a neural operator restores the resolution that governs pool geometry.

This paper therefore considers a finite-volume model of the melt pool in laser manufacturing. The material is represented by its thermophysical properties [24], and the numerical experiments use experimentally validated parameters. The work proceeds in two steps. First, on 156 converged cases, one direction is coarsened at a time to obtain the sensitivity of the melt-pool engineering quantities to resolution along the weld, across the half-width and through the thickness, and this sensitivity is compared with the boundary-layer scales. Second, a neural network is then used for a multiphysics correction, recovering the flow and temperature information lost in the unresolved free-surface viscous shear layer and thereby repairing the melt width. The correction is implemented with a Fourier neural operator. The scored quantities are the melt-pool length, half-width, depth, liquid volume and peak magnesium concentration. The whole-domain temperature R^2 is not used: the solid far field lies close to the preheat temperature and would inflate that metric without providing information on weld quality.

Section 2 presents the thermo-fluid-solute model, properties and boundary conditions. Section 3 measures the resolution demand. Section 4 gives the numerical

procedure and uncertainty. Section 5 reconstructs the reference field from the coarse solution and reports the results. Section 6 concludes.

2 Thermo-fluid-solute model of hybrid laser–MIG welding

2.1 Process and materials

The configuration follows Chen et al. [19]. The base metal is A7N01 aluminium alloy and the filler is ER5356 wire of diameter $\phi 1.2\,\mathrm{mm}$. In the solute model the filler is treated as 95% Al–5% Mg and the base metal as 95.5% Al–4.5% Zn [25]. The computational domain is $44\,\mathrm{mm} \times 10\,\mathrm{mm} \times 6\,\mathrm{mm}$, using symmetry about the weld centreline so that only half of the workpiece is discretised. The nominal condition is laser power 1000 W, welding current 150 A, wire feed rate $9.3\,\mathrm{m\,min^{-1}}$, laser–MIG separation 2 mm, torch tilt 22° and travel speed $18\,\mathrm{mm\,s^{-1}}$ along a linear bead-on-plate path. The solidus and liquidus temperatures are 858 K and 923 K. The solver has already been validated for this material and parameter combination [19].

2.2 Governing equations

The liquid is treated as Newtonian, incompressible and laminar. In a frame translating with the torch at speed V, continuity, momentum, energy and species transport are

$$\frac{\partial \rho}{\partial t} + \frac{\partial (\rho u_i)}{\partial x_i} = 0, \tag{1}$$

$$\begin{aligned} \frac{\partial (\rho u_i)}{\partial t} + \frac{\partial (\rho u_i u_j)}{\partial x_j} &= \frac{\partial}{\partial x_j}\left(\mu \frac{\partial u_i}{\partial x_j}\right) - \frac{\partial p}{\partial x_i} + \frac{\partial}{\partial x_j}\left(\mu \frac{\partial u_j}{\partial x_i}\right) \\ &\quad - V \frac{\partial (\rho u_i)}{\partial x} - C_0 \frac{(1-f_\ell)^2}{f_\ell^3 + B} u_i + F_i, \end{aligned} \tag{2}$$

$$\begin{aligned} \frac{\partial (\rho h)}{\partial t} + \frac{\partial (\rho u_i h)}{\partial x_i} &= \frac{\partial}{\partial x_i}\left(\frac{k}{C_p} \frac{\partial h}{\partial x_i}\right) - \frac{\partial (\rho \Delta H)}{\partial t} - \frac{\partial (\rho u_i \Delta H)}{\partial x_i} \\ &\quad - V \frac{\partial (\rho h)}{\partial x} - V \frac{\partial (\rho \Delta H)}{\partial x} + Q_{\mathrm{laser}}, \end{aligned} \tag{3}$$

$$\begin{aligned} \frac{\partial (\rho C)}{\partial t} + \frac{\partial (\rho u_i C)}{\partial x_i} &= \frac{\partial}{\partial x_i}\left(\rho D \frac{\partial C}{\partial x_i}\right) + \frac{\partial}{\partial x_i}\left(\rho D \frac{\partial (C_\ell - C)}{\partial x_i}\right) \\ &\quad - \frac{\partial}{\partial x_i}\left(\rho f_s (C_\ell - C_s) u_i\right). \end{aligned} \tag{4}$$

The Carman–Kozeny term suppresses velocity in the mushy zone, F_i collects buoyancy and electromagnetic forces, Q_{laser} is the volumetric laser source including Fresnel absorption and multiple reflection in the keyhole, and C is the magnesium mass fraction. The discrete solution on the structured mesh is the five-component array $U = (u, v, w, T, C) \in \mathbb{R}^{I \times J \times K \times 5}$. The solver uses the temperature-dependent properties of Ref. [19]. Table 1 lists representative constant values.

Table 1 Representative constant properties used for the scale estimates in Section 3.1.

Quantity	Symbol	Value	Unit
Solid-density scale	ρ	2700	$\mathrm{kg\,m^{-3}}$
Liquid-density scale	ρ_ℓ	2400	$\mathrm{kg\,m^{-3}}$
Specific heat	C_p	900	$\mathrm{J\,kg^{-1}\,K^{-1}}$
Thermal conductivity	k	170	$\mathrm{W\,m^{-1}\,K^{-1}}$
Dynamic viscosity	μ	1.3×10^{-3}	$\mathrm{Pa\,s}$
Mg diffusivity in the liquid	D	5×10^{-9}	$\mathrm{m^2\,s^{-1}}$
Solidus / liquidus	T_s, T_l	858, 923	K

2.3 Boundary conditions

The thermal and mechanical boundary conditions are those of Ref. [19]; only the parts that bear on mesh resolution are restated here. The computation is performed in a frame translating with the torch at speed V. The weld centreline $y = 0$ is a symmetry plane: the normal velocity vanishes and the temperature and solute fluxes are zero. Combined convection and radiation cool the solid outer surfaces. Marangoni shear, arc pressure and droplet impact act on the free surface; the droplets also supply mass and a magnesium source. Laser energy enters the energy equation as a volumetric source that includes Fresnel absorption and multiple reflection in the keyhole. The MIG arc heat source is that of Ref. [19]. These boundaries fix the energy and mass input on the conservative backbone, so the correction in Section 5 does not redistribute the heat sources: it only reconstructs the field content lost when the mesh is coarsened.

2.4 Reference mesh

The reference solution is computed on a $292 \times 34 \times 41$ mesh. I along the weld, J across the half-width, and K through the thickness. This resolution is used because the solution on this mesh agrees with experiment [19]. The mesh is both graded and body-fitted: the I and J nodes are clustered toward the weld, while the K nodes vary with (x, y) to conform to the deformed free surface. There is therefore no single Δx, Δy, or Δz. Throughout, resolution is discussed in terms of the **near-weld median spacing**

$$\Delta x \approx 143\,\mu\mathrm{m}, \qquad \Delta y \approx 150\,\mu\mathrm{m}, \qquad \Delta z \approx 95\,\mu\mathrm{m}. \tag{5}$$

The workpiece top surface lies at $z \approx 5.9685\,\mathrm{mm}$ near the weld. The fusion boundary is located by linear interpolation of the $T = T_s$ crossing between neighbouring nodes, so as to remove the quantisation error of a nodal threshold.

3 Measurement of the resolution demand

This section measures how much melt-pool information remains after a computed fine-mesh solution is coarsened, and hence where nodes should be spent.

3.1 Which scale is actually under-resolved

From Table 1, $\alpha = k/(\rho C_p)$ and $\nu = \mu/\rho_\ell$ give $\alpha \approx 7 \times 10^{-5}\,\mathrm{m^2\,s^{-1}}$ and $\nu \approx 5.4 \times 10^{-7}\,\mathrm{m^2\,s^{-1}}$, so $Le \approx 1.4 \times 10^4$ and $Pr \approx 8 \times 10^{-3}$. The pool length and peak liquid velocity are the nominal values $L \approx 16\,\mathrm{mm}$ and $u_{\max} = 1.26\,\mathrm{m\,s^{-1}}$ from Refs. [19, 26],

$$Pe_T \approx 3 \times 10^2, \qquad Re \approx 3.7 \times 10^4, \qquad Pe_C \approx 4 \times 10^6, \tag{6}$$

corresponding to $\delta \sim L\,Pe^{-1/2}$. Liquid-metal $Pr \ll 1$ ranks the thermal, viscous and solutal layers as $\delta_T > \delta_\nu > \delta_C$; lengths and cell counts are in Table 2.

The mushy-front thickness is $(T_l - T_s)/|\nabla T|$, and the gradient must be the local value on the fusion surface. The median thickness over fusion-surface nodes on 156 cases is in Table 2; the steepest 1% is $139\,\mu\mathrm{m}$. Replacing the local gradient by a domain-wide temperature drop over the pool depth folds far-field decay into the fusion-surface gradient, underestimates the thickness by about an order of magnitude, and misidentifies the thickness direction as the starved one.

Table 2 Resolution of the characteristic lengths on the $292 \times 34 \times 41$ graded mesh. Spacings are near-weld medians.

Scale	Mechanism	Length	Reference spacing	Cells
ℓ_I	convected thermal wake α/V	3.9 mm	$\Delta x = 143\,\mu\mathrm{m}$	≈ 27
ℓ_J	Marangoni cell $W/2$ (geometric extent)	3 mm	$\Delta y = 150\,\mu\mathrm{m}$	≈ 20
ℓ_{mushy}	mushy front, measured	$675\,\mu\mathrm{m}$	$\Delta z = 95\,\mu\mathrm{m}$	≈ 7
δ_T	thermal boundary layer	0.9 mm	Δy	≈ 6
δ_ν	viscous shear layer	$83\,\mu\mathrm{m}$	Δy	0.55
δ_C	solutal boundary layer	$8\,\mu\mathrm{m}$	Δy	0.05

Of the six scales, only the viscous shear layer and the solute layer occupy less than one cell, and both lie in the half-width direction: the former carries the surface circulation that sets the melt width, the latter cuts off the peak concentration. The shear layer is driven by free-surface shear, in which Marangoni forcing usually dominates, with contributions from arc shear and droplet impact (Section 2.3). The estimate δ_ν is based on $u_{\max}$ and does not itself distinguish the driving mechanism, so the attribution of directional sensitivity in this paper is taken from the factorial data of Section 3.2; the scale analysis supplies the mechanistic interpretation. The mushy front is already resolved, so the thickness direction is not the starved one.

3.2 One-direction coarsening

Each of 156 converged finite-volume cases contributes three snapshots, giving 468 samples. The percentages in Table 3 are the arithmetic mean, over these 156 cases, of the relative error of each listed mesh against $292 \times 34 \times 41$.

Against $292 \times 34 \times 41$, the melt-width error is 1.27% on $292 \times 17 \times 41$, 0.03% on $146 \times 34 \times 41$ and 0.16% on $292 \times 34 \times 20$, so $1.27/0.03 \approx 42$ and $1.27/0.16 \approx 8$. Liquid-volume errors on those three meshes are 2.39%, 0.31% and 0.24%. Melt-depth errors

Table 3 Relative error of each listed mesh against $292 \times 34 \times 41$; arithmetic mean over 156 cases (468 samples). I, J and K are the node counts along the weld, half-width and thickness; columns are melt length, half-width, depth, liquid volume and peak magnesium concentration.

Mesh $I \times J \times K$	Cell fraction	L	$W/2$	D_p	$\mathcal{V}_\ell$	C_max
$146 \times 34 \times 41$ (I only)	0.500	0.18%	0.03%	0.10%	0.31%	0.09%
$292 \times 17 \times 41$ (J only)	0.500	0.02%	1.27%	0.00%	2.39%	0.02%
$292 \times 34 \times 20$ (K only)	0.488	0.14%	0.16%	0.26%	0.24%	0.47%
$146 \times 17 \times 41$	0.250	0.17%	1.28%	0.10%	2.67%	0.10%
$146 \times 17 \times 20$	0.122	0.19%	1.53%	0.27%	2.82%	0.50%
$73 \times 8 \times 20$	0.029	0.59%	5.05%	0.45%	6.91%	0.83%
$73 \times 8 \times 10$	0.014	1.24%	6.22%	0.74%	6.96%	1.15%

are 0.00%, 0.10% and 0.26%, all $\leq 0.26\%$, consistent with a 7-cell mushy front. The melt-width error on $146 \times 17 \times 41$ is 1.28%, almost the same as 1.27% on $292 \times 17 \times 41$; reducing the weld direction from 292 to 146 nodes adds almost no extra melt-width error.

Fig. 1 plots the one-direction rows of Table 3 as a bar chart: melt-width and liquid-volume errors concentrate in the coarsened-J column, while every bar for coarsened I or K remains below 0.5%.

The C_max column marks the limit of the scale analysis: the solute layer δ_C occupies only 0.05 cells in J and is the most under-resolved, yet C_max is almost insensitive to coarsening J (0.02%) and is most sensitive to K (0.47%). The peak concentration sits in the droplet-impact region and is set by the solute source and bulk mixing, not by resolution of the solute boundary layer. An under-resolved thin layer in a given direction therefore need not make that direction sensitive; the directional ranking is established by the factorial data of Table 3, and the scales of Section 3.1 are used to interpret rather than to infer it.

Implication for mesh design. If the computational budget is limited, refinement should be given first to the near-weld spacing in the half-width direction, not to the thickness. Penetration is set by the integrated energy balance, not by the local thickness of the mushy zone.

3.3 Grid sensitivity of the engineering quantities

All five columns of Table 3 are scored against $292 \times 34 \times 41$. On $73 \times 8 \times 10$ they are

$$L = 1.24\%, \quad W/2 = 6.22\%, \quad D_\mathrm{p} = 0.74\%, \quad \mathcal{V}_\ell = 6.96\%, \quad C_\mathrm{max} = 1.15\%. \tag{7}$$

Melt width and liquid volume are about 6–7%; melt length, depth and C_max are about 0.7–1.2%, an order of magnitude smaller. All five columns degrade monotonically as the mesh is coarsened, and all five coincide with the reference when the mesh is returned to $292 \times 34 \times 41$.

Against $292 \times 34 \times 41$, melt width and liquid volume are 1.27% and 2.39% on $292 \times 17 \times 41$, and 0.03% and 0.31% on $146 \times 34 \times 41$; the former are $1.27/0.03 \approx 42$

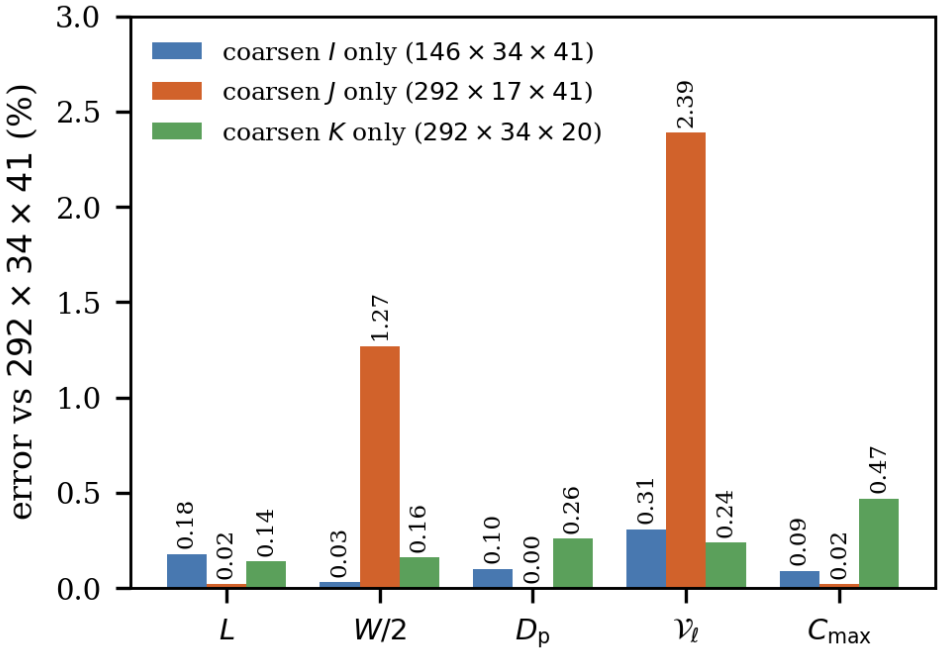


Fig. 1 Directional sensitivity under one-direction coarsening (first three rows of Table 3): each bar is the mean error over 156 cases relative to $292 \times 34 \times 41$. Melt width and liquid volume are sensitive almost only to the half-width direction J.

and $2.39/0.31 \approx 8$ times the latter. On $73 \times 8 \times 20$ the two columns rise to 5.05% and 6.91%. The circulation that sets the melt width is still present on $292 \times 34 \times 41$; after the half-width is reduced from 34 to 17 nodes it no longer fits, and lifting leaves a residual that grows as resolution is lost. Section 5 tests the correction on these two quantities only.

The nature of these percentages needs emphasis. The errors in Table 3 are the difference between each listed-mesh solution and the $292 \times 34 \times 41$ solution, that is, the numerical bias introduced by coarsening, not a physical error relative to experiment. The experimental validation holds on $292 \times 34 \times 41$; the part by which the coarse solution departs from it grows monotonically with coarsening (all five columns of Table 3) and is a systematic discretisation bias without experimental warrant. The 5–6% of the coarse field should therefore not be judged against an engineering tolerance as if it were "good enough": it is a numerical bias that can and should be removed. The aim of the correction is to return as close as possible to the $292 \times 34 \times 41$ solution.

4 Numerical procedure

4.1 Case library

The same solver is run at $P = 1000$–$2000\,\mathrm{W}$ and $V = 0.006$–$0.024\,\mathrm{m\,s^{-1}}$ on the $292 \times 34 \times 41$ mesh, with six snapshots per operating point, giving 156 converged cases. At $t = 0.255\,\mathrm{s}$ the penetration is only about 0.04 mm and relative errors are unstable, so only the three snapshots with $t \geq 1.0\,\mathrm{s}$ are used (468 samples).

Fig. 2 shows YZ sections at the heat source for three cases at $t = 1.505\,\mathrm{s}$: the half-domain is mirrored about $Y = 0$, with temperature contours and velocity vectors. The top row is the $292 \times 34 \times 41$ reference; the middle row is the $73 \times 8 \times 20$ field of the same case; the bottom row is the absolute temperature difference on that coarse mesh (the difference between the coarse-node temperature and the maximum fine-mesh temperature in the same cell; rainbow scale 0–400 K, saturating in the keyhole).

4.2 Experimental setup

The correction in Section 5 is applied mainly on $73 \times 8 \times 20$, whose cell count is 2.9% of $292 \times 34 \times 41$. The aim is to bring the field on this coarse mesh closer to the $292 \times 34 \times 41$ reference with a neural operator. Each field is standardised separately before fitting. First-order gradient descent is used, with a cosine-decayed learning rate and a batch of two samples; training runs for at most 400 epochs and stops if there is no improvement for 120 consecutive epochs. Each scheme is repeated from three initialisations; the main text reports the mean $\pm$ standard deviation, to show whether the result is stable under a change of initialisation.

On cost: training the correction operator uses 156 fine-mesh cases. That outlay is incurred once, and pays only when many repeated evaluations are required—process-window scans, parameter optimisation and online process control often need hundreds or thousands of melt-pool solves. After the training set has been amortised, each new case needs only a coarse solve at 2.9% of the fine-mesh cell count plus one operator evaluation. The extrapolation test on 48 unseen cases in Section 5.4 is exactly this amortised setting. If only a few cases are needed, the fine mesh is cheaper and the present method does not apply.

5 Reconstructing the reference field from the coarse solution

5.1 Finite-volume coarse field and correction

The directional audit in Section 3 shows that engineering quantities such as melt width are most sensitive to half-width resolution and far less sensitive to the weld and thickness directions. A Fourier neural operator is therefore used for a coarse-to-fine correction that serves the pool geometry rather than equal refinement in all three directions. Finite-volume computation on the working mesh produces the coarse field U_c. After trilinear lifting $\mathcal{I}(U_\mathrm{c})$ to $292 \times 34 \times 41$, the correction is

$$U_\mathrm{f} \approx \mathcal{I}(U_\mathrm{c}) + m_\ell \odot \mathcal{R}_\theta(U_\mathrm{c}). \tag{8}$$

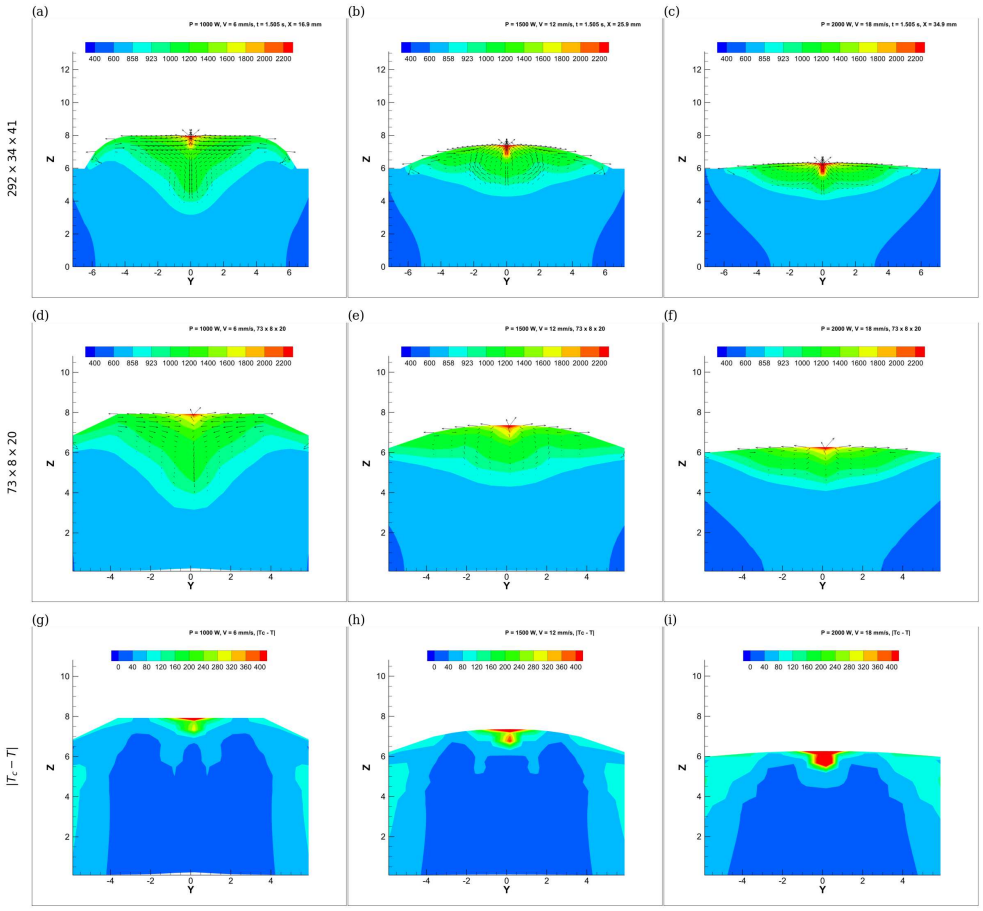


Fig. 2 YZ sections at the heat source. (a–c) temperature and velocity on $292 \times 34 \times 41$; (d–f) the $73 \times 8 \times 20$ field of the same case; (g–i) $|T_c - T|$, rainbow scale 0–400 K. (a,d,g) 1000 W, 6 mm s^{-1}; (b,e,h) 1500 W, 12 mm s^{-1}; (c,f,i) 2000 W, 18 mm s^{-1}. The half-domain is mirrored about $Y = 0$. All frames are at $t = 1.505$ s.

The operator does not receive (P, V): the operating point is already in the coarse field. Retaining $\mathcal{I}$ as an additive backbone is consistent with multifidelity corrections that use a cheap approximation to adjust a high-fidelity output [27–29].The aim is to correct the finite-volume coarse field toward $292 \times 34 \times 41$; Section 5.2 gives the example used in this paper.

5.2 A Fourier neural operator as one example

The operator, the mode budget and the solute treatment can all be chosen differently when the reference field is reconstructed from the coarse solution, for example a physics-informed network [30–32] or a data-driven surrogate of pool geometry [33, 34]. The example used here takes a Fourier neural operator [35] as $\mathcal{R}_\theta$ (DeepONet [36] is a related operator) and writes the three directions as explicit truncations m_I, m_J, m_K,

so that the node budget of Section 3 can be entered. The shared backbone is $(8, 6, 6)$: only low modes in all three directions, slightly more along the weld and not concentrated on the thickness. Each of the five fields then receives its own truncation, placing extra modes on the axis along which that field varies most, Table 4. The cross-width velocity v is given the highest J-budget, matching the melt-width sensitivity to the half-width in Table 3; u and T are elongated along the weld; w descends through the thickness.

The five fields may be fed to the operator together; the per-field budgets are in Table 4.

Table 4 Per-field resolution budget used in this example.

Field	(m_I, m_J, m_K)	Rationale
u	$(8, 4, 4)$	streamwise jet along the weld
v	$(4, 8, 4)$	Marangoni return across the half-width
w	$(4, 4, 8)$	downwelling at the keyhole root
T	$(8, 4, 4)$	thermal wake already resolved along I
C	$(6, 6, 8)$	solute layer through the thickness

5.3 Spectra along the mesh directions I, J and K

Table 3 is already a model-free baseline. Fig. 3 shows the mean one-dimensional spectra of T, $|\mathbf{u}|$ and C in the reference solution along the three mesh directions (the I, J and K nodes): temperature decays slowly along I and rapidly along J and K; the velocity magnitude decays most slowly along J, consistent with δ_ν; concentration has the heaviest tail along the nodal directions. The spectra are computed from the finite-volume solution and do not involve a learned model.

5.4 Lift-correction results on the extrapolation set

Table 5 compares process variants in which all five fields are fitted together. The complete correction with C frozen is shown in Fig. 4 (Section 5.5).

The unseen extrapolation set comprises 48 cases with three snapshots at $t \geq 1\,\mathrm{s}$ per case. Table 5 scores the same $73 \times 8 \times 20$ coarse fields against $292 \times 34 \times 41$, with the training setup of Section 4.2. The rows are:

- Trilinear lift: no neural operator; the coarse field is interpolated onto the fine mesh.
- Directional budget of Table 4: each of u, v, w, T, C uses one (m_I, m_J, m_K) set from Table 4, the example of Section 5.2.
- Shared $(8, 6, 6)$: the five fields share one truncation, with no per-field allocation.
- Isotropic $(8, 8, 8)$: the same truncation count in all three directions.

Melt width falls from 5.16% to 2.38% and liquid volume from 6.51% to 2.63%: the operator of Table 4 brings the coarse field closer to $292 \times 34 \times 41$. All physical quantities improve on the uncorrected lift, so the neural operator is effective. Melt

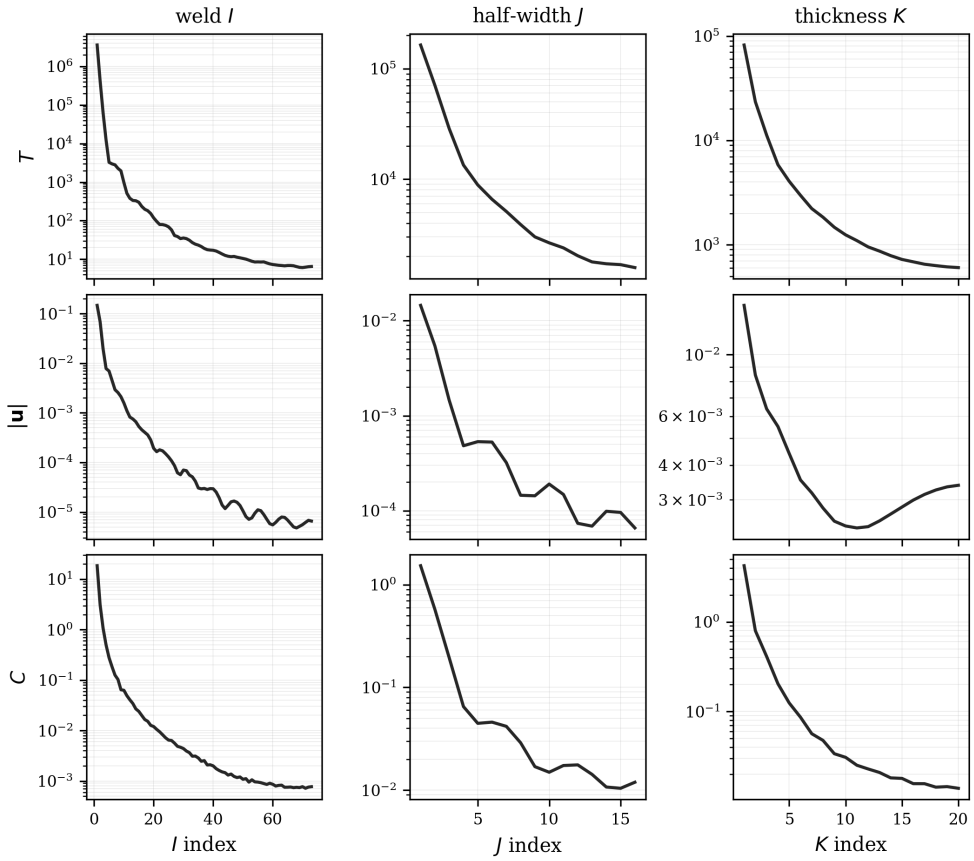


Fig. 3 Mean one-dimensional spectra of temperature, velocity magnitude and magnesium concentration in the reference solution along the mesh directions I, J and K. I, J and K are the nodal directions along the weld, half-width and thickness. The spectra are computed directly from the finite-volume solution and do not involve a learned model.

length and depth already have small errors, change little after the lift correction, and are not particularly sensitive to the mesh.

Solute does not behave well: when all five fields are fitted together, $C_{\max}$ rises from the lifted 0.90% to about 20–30% (Table 5); a soft liquid mask still gives 7.12%. This paper therefore recommends freezing C at $\mathcal{I}(U_c)$ and correcting only u, v, w, T.

5.5 Correction with solute frozen

This is the complete implementation in the present example. Fig. 4 places the fine field, the coarse field and $|T_c - T|$ of Fig. 2 on the same row as the correction with C frozen: three unseen extrapolation cases, from left to right $292 \times 34 \times 41$, $73 \times 8 \times 20$, $|T_c - T|$, the field restored to the fine mesh, and the remaining $|T_{\text{corr}} - T|$ (difference of cell-wise maxima, same colour scale as Fig. 2). The middle row is $P = 2000\,\text{W}$, $V = 15\,\text{mm}\,\text{s}^{-1}$; the top and bottom rows are low- and high-heat-input extrapolation.

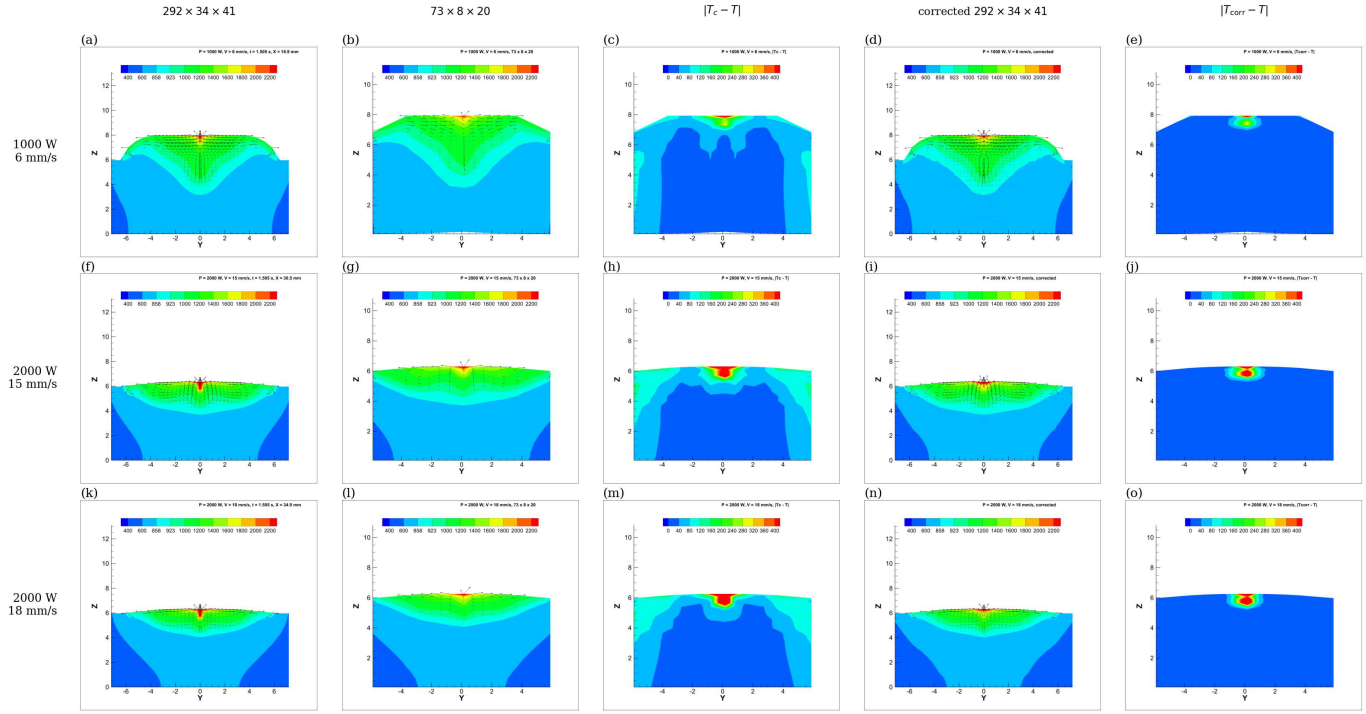


Fig. 4 YZ section at the heat source on unseen extrapolation cases, coarse-to-fine correction with C frozen. Rows correspond to the three (P, V) cases; columns, left to right, are the $292 \times 34 \times 41$ reference, the $73 \times 8 \times 20$ coarse field, $|T_{\mathrm{c}} - T|$, the corrected field and $|T_{\mathrm{corr}} - T|$. Error columns are the difference of cell-wise maxima, rainbow scale 0–400 K. (a–e) 1000 W, 6 mm s^{-1}; (f–j) 2000 W, 15 mm s^{-1}; (k–o) 2000 W, 18 mm s^{-1}. All at $t = 1.505$ s.

Table 5 Extrapolation set (48 cases, 144 snapshots), $73 \times 8 \times 20$, three seeds.

Budget	L	$W/2$	D_{p}	$\mathcal{V}_{\ell}$	$C_{\max}$
Trilinear lift	0.61%	**5.16%**	0.50%	6.51%	0.90%
Table 4 directional	0.56 ± 0.07	$\mathbf{2.38 \pm 0.35}$	0.55 ± 0.29	2.63 ± 0.20	28.0 ± 1.3
Shared $(8, 6, 6)$	0.65 ± 0.10	2.65 ± 0.51	0.72 ± 0.02	2.74 ± 0.10	32.5 ± 12.3
Isotropic $(8, 8, 8)$	0.60 ± 0.04	2.88 ± 0.19	0.95 ± 0.19	2.65 ± 0.05	32.9 ± 6.5

After correction the pool geometry has returned to the fine-mesh reference: the spread-out $|T_{\mathrm{c}} - T|$ collapses to a small patch at the heat source, and on the 48 unseen cases melt width falls from 5.16% to 2.38% and liquid volume from 6.51% to 2.63%.

6 Conclusions

A directional resolution audit is carried out for a finite-volume melt-pool model in laser manufacturing, and a neural network is then used for the correction. The main conclusions are as follows.

1. The half-width is the most sensitive direction. On 156 cases, doubling the J resolution returns about 40 times the melt-width benefit of the same refinement in I.
2. For example, melt width is limited by the unresolved free-surface viscous shear layer. Recovering the flow and temperature information lost in that layer repairs the melt width.
3. After the neural network corrects velocity and temperature, the melt-width error is reduced by 53.9% and the liquid-volume error by 59.6%.

Melt-pool simulation in laser manufacturing therefore no longer needs to take equal refinement in all three directions as the default mesh. Resolution should be allocated according to the directional sensitivity of the engineering quantities, placing the limited nodes in the direction that actually governs the pool geometry. Where repeated solutions are required, as in process-window scans, parameter optimization and online control, the conservative computation can remain on an affordable mesh and a neural operator can correct the physical fields, so that the computational budget is reduced substantially. The boundary of this approach is equally clear: it inherits the conservation structure of a validated model and can recover only the geometric information lost to coarsening. It cannot rewrite composition that is set by source terms and bulk transport.

Acknowledgements. The authors thank the Chinese Academy of Sciences for its support.

Funding Declaration. This work was funded by the National Science and Technology Major Project and the Talent Program of the Chinese Academy of Sciences (Grant No. 492025000127).

Conflicts of Interests. The authors declare that there are no known conflicts of interest, including any intellectual property disputes, that could have influenced the work reported in this paper.

Data availability. The datasets used and/or analysed during the current study available from the corresponding author on reasonable request.

References

[1] Ribic, B., Palmer, T. A. & DebRoy, T. Problems and issues in laser-arc hybrid welding. *International Materials Reviews* **54**, 223–244 (2009).

[2] Liu, S., Li, J., Mi, G., Wang, C. & Hu, X. Study on laser-MIG hybrid welding characteristics of A7N01-T6 aluminum alloy. *The International Journal of Advanced Manufacturing Technology* **87**, 1135–1144 (2016).

[3] Zhang, Z. & Wu, C. S. Effect of fluid flow in the weld pool on the numerical simulation accuracy of the thermal field in hybrid welding. *J. Manuf. Process.* **20**, 215–223 (2015).

[4] Shu, Y. *et al.* A critical look at the prediction of the temperature field around a laser-induced melt pool on metallic substrates. *Scientific Reports* **11**, 12224 (2021).

[5] Cho, W.-I., Na, S.-J., Thomy, C. & Vollertsen, F. Numerical simulation of molten pool dynamics in high power disk laser welding. *Journal of Materials Processing Technology* **212**, 262–275 (2012).

[6] Zhou, J. & Tsai, H. Modeling of transport phenomena in hybrid laser-mig keyhole welding. *International Journal of Heat and Mass Transfer* **51**, 4353–4366 (2008).

[7] Piekarska, W. & Kubiak, M. Three-dimensional model for numerical analysis of thermal phenomena in laser–arc hybrid welding process. *International Journal of Heat and Mass Transfer* **54**, 4966–4974 (2011).

[8] Cho, D.-W., Cho, W.-I. & Na, S.-J. Modeling and simulation of arc: Laser and hybrid welding process. *J. Manuf. Process.* **16**, 26–55 (2014).

[9] He, X., Fuerschbach, P. W. & DebRoy, T. Heat transfer and fluid flow during laser spot welding of 304 stainless steel. *Journal of Physics D: Applied Physics* **36**, 1388–1398 (2003).

[10] Rai, R., Elmer, J. W., Palmer, T. A. & DebRoy, T. Heat transfer and fluid flow during keyhole mode laser welding of tantalum, Ti–6Al–4V, 304L stainless steel and vanadium. *Journal of Physics D: Applied Physics* **40**, 5753–5766 (2007).

[11] Farzadi, A., Serajzadeh, S. & Kokabi, A. Investigation of weld pool in aluminum alloys: Geometry and solidification microstructure. *International Journal*

of Thermal Sciences **49**, 809–819 (2010).

[12] Duggirala, A., Kalvettukaran, P., Acherjee, B. & Mitra, S. Numerical simulation of the temperature field, weld profile, and weld pool dynamics in laser welding of aluminium alloy. *Optik* **247**, 167990 (2021).

[13] Liu, C. *et al.* Numerical analysis of the formation mechanism of high back penetration depth of thin plate aluminum alloy in mig welding. *Applied Thermal Engineering* **262**, 125264 (2025).

[14] Lei, Z. *et al.* Numerical study of thermal fluid dynamics in laser welding of al alloy with powder feeding. *Applied Thermal Engineering* **151**, 394–405 (2019).

[15] Jing, H. *et al.* Effect of weld pool flow and keyhole formation on weld penetration in laser-mig hybrid welding within a sensitive laser power range. *Applied Sciences* **12** (2022).

[16] Huang, S. *et al.* Keyhole-induced pore formation mechanism in laser-mig hybrid welding of aluminum alloy based on experiment and multiphase numerical model. *Journal of Materials Processing Technology* **314**, 117903 (2023).

[17] Liu, W. *et al.* Evolution of melt pool motion and temperature field based on powder scale modeling during laser directed energy deposition process. *Applied Thermal Engineering* **243**, 122564 (2024).

[18] Cao, X., Duan, C., Luo, X., Xu, H. & Hao, X. Integrated framework of multiphysics mechanism models for gas-powder flow, molten pool evolution and part deformation in high alloy steel additive manufacturing process. *Applied Thermal Engineering* **257**, 124462 (2024).

[19] Chen, X., Yu, G., He, X., Li, S. & Li, Z. Numerical study of heat transfer and solute distribution in hybrid laser-mig welding. *International Journal of Thermal Sciences* **149**, 106182 (2020).

[20] DebRoy, T. *et al.* Additive manufacturing of metallic components – process, structure and properties. *Progress in Materials Science* **92**, 112–224 (2018).

[21] Alauzet, F. & Loseille, A. A decade of progress on anisotropic mesh adaptation for computational fluid dynamics. *Computer-Aided Design* **72**, 13–39 (2016). 23rd International Meshing Roundtable Special Issue: Advances in Mesh Generation.

[22] Frey, P. & Alauzet, F. Anisotropic mesh adaptation for cfd computations. *Computer Methods in Applied Mechanics and Engineering* **194**, 5068–5082 (2005). Unstructured Mesh Generation.

[23] Hamide, M., Massoni, E. & Bellet, M. Adaptive mesh technique for thermal–metallurgical numerical simulation of arc welding processes. *International*

Journal for Numerical Methods in Engineering **73**, 624–641 (2008).

[24] Miyagi, M. *et al.* Effect of alloy element on weld pool dynamics in laser welding of aluminum alloys. *Scientific Reports* **8**, 12944 (2018).

[25] Miao, H., Yu, G., He, X., Li, S. & Chen, X. Comparative study of hybrid laser–MIG leading configuration on porosity in aluminum alloy bead-on-plate welding. *The International Journal of Advanced Manufacturing Technology* **91**, 2681–2688 (2017).

[26] Chen, X., Yu, G., He, X. & Li, S. Investigation of thermal dynamics for different leading configuration in hybrid laser-mig welding. *Optics & Laser Technology* **134**, 106567 (2021).

[27] Kennedy, M. & O'Hagan, A. Predicting the output from a complex computer code when fast approximations are available. *Biometrika* **87**, 1–13 (2000).

[28] Forrester, A. I. J., Sóbester, A. & Keane, A. J. Multi-fidelity optimization via surrogate modelling. *Proceedings of the Royal Society A: Mathematical, Physical and Engineering Sciences* **463**, 3251–3269 (2007).

[29] Peherstorfer, B., Willcox, K. & Gunzburger, M. Survey of multifidelity methods in uncertainty propagation, inference, and optimization. *SIAM Review* **60**, 550–591 (2018).

[30] Raissi, M., Perdikaris, P. & Karniadakis, G. Physics-informed neural networks: A deep learning framework for solving forward and inverse problems involving nonlinear partial differential equations. *Journal of Computational Physics* **378**, 686–707 (2019).

[31] Cao, X. *et al.* Physics-informed machine learning approach for molten pool morphology prediction and process evaluation in directed energy deposition of 12crni2 alloy steel. *Journal of Manufacturing Processes* **119**, 806–826 (2024).

[32] Peng, S. *et al.* Prediction of 3d temperature field through single 2d temperature data based on transfer learning-based pinn model in laser-based directed energy deposition. *Journal of Manufacturing Processes* **138**, 140–156 (2025).

[33] Zhang, Z., Wang, Z., Cui, X., Zheng, Y. & Wang, D. A physics-aware autoregressive encoder–decoder for fast surrogate prediction of transient melt pool dynamics in laser welding and additive manufacturing. *Journal of Manufacturing Processes* **170**, 228–248 (2026).

[34] Duggirala, A., Acherjee, B. & Mitra, S. Predicting weld pool metrics in laser welding of aluminum alloys using data-driven surrogate modeling: A fea-doe-gprn hybrid approach. *Proceedings of the Institution of Mechanical Engineers, Part E: Journal of Process Mechanical Engineering* **240**, 1350–1364 (2026).

[35] Li, Z. *et al.* Fourier neural operator for parametric partial differential equations. *International Conference on Learning Representations* (2021).

[36] Lu, L., Jin, P., Pang, G., Zhang, Z. & Karniadakis, G. E. Learning nonlinear operators via DeepONet based on the universal approximation theorem of operators. *Nature Machine Intelligence* **3**, 218–229 (2021).